

18 **Abstract**

19 High-quality magnetic data are important in guiding new knowledge of the solid earth in frontier
20 regions, such as Antarctica, where these data are often among the first data collected. The
21 difficulties of data collection in remote regions often lead to less than ideal data collection, leading
22 to data that are sparse and four-dimensional in nature. Standard aeromagnetic data collection
23 procedures are optimised for the (nearly) 2D data that are collected in industry-standard surveys. In
24 this work we define and apply a robust magnetic data correction approach that is optimised to these
25 four dimensional data. Data are corrected in three phases, first with operations on point data,
26 correcting for spatio-temporal geomagnetic conditions, then operations on line data, adjusting for
27 elevation differences along and between lines and finally a line-based levelling approach to bring
28 lines into agreement while preserving data integrity. For a large-scale East Antarctic survey,
29 comparison with more traditional processing approaches demonstrates superiority, gains in this case
30 are relatively marginal for phase 1 (3-5%) but more substantial for phase 2 (10-35%). For the full
31 implementation, median cross-tie error reduction is 89%, reaching a final error of 8-9 nT. Residual
32 errors are attributed to limitations in the models used for in predicting the 4D geomagnetic
33 conditions and also some limitations of the inversion process used in phase 2. Nevertheless, data
34 have improved utility for tectonic and glacio-tectonic interpretation and modelling, in particular
35 quantitative approaches, which are enabled with less bias and more confidence compared to
36 conventional processing.

37 **Plain Language Summary**

38 Observations of the Earth's magnetic field underpin our knowledge of geology and tectonics, and are
39 often among the first data collected in frontier regions. This work focuses on the problems
40 experienced in remote surveys, including observation periods extending over years, rather than
41 days, and flying heights that vary over kilometres, rather than metres. Conventional approaches are
42 inappropriate for these data and a new way to process airborne or marine observations of magnetic
43 field intensity is developed and tested. Applied to a dataset in East Antarctica, the data quality is
44 substantially improved and the data better reveals the geology hidden beneath the ice of Antarctica.

45 **Index Terms**

46 0925, 0910, 0903

47 **1 Introduction**

48 Since the beginnings of plate tectonic theory, observations of the Earth's magnetic field have been
49 essential to understanding the structure and evolution of both continents and oceans [*Behrendt and*
50 *Watorson, 1970; Vine and Matthews, 1963*]. Commonly, magnetic data is one of the first geophysical
51 data sets collected, forming the basis for subsequent investigations of the solid earth with other
52 techniques. Good quality data is essential for the robust interpretation of tectonic systems, including
53 the identification of major tectonic structures, and the internal structuring of tectonic domains, the
54 definition of sedimentary basins, and clear mapping of magnetic polarity reversals in the oceanic
55 crust.

56 In many parts of the world, in particular in regions with resource exploration activity, magnetic data
57 has been systematically collected in regular surveys [*Nabighian et al., 2005*]. High Resolution
58 Aeromagnetic (HRAM) Data is collected at low-flying heights, often < 100m, consistently draped over
59 topography and with individual surveys occurring over a short time period. Lines are arranged in
60 parallel arrays, with spacings often < 1 km. For these surveys, robust data processing workflows

61 exist, being well suited to the survey design and goals typically resulting in a representative data-grid
62 [Nabighian *et al.*, 2005]. Either the original line data or the regular grids can then be interpreted and
63 modelled to provide knowledge of the solid Earth.

64 In other parts of the world, for example in marine or frontier regions, data like these are not widely
65 available either due to a lack of surveying or due to data being proprietary, and the only data
66 available are often from large-scale reconnaissance surveys. These regions are where we, in general,
67 know least about the magnetic structure of the solid earth, and so there is a need to maximise the
68 value of these surveys. Datasets in these regions are defined, overall, by more irregular line
69 directions and spacings, very variable flying heights and terrain separations and by much longer
70 time-frames of data collection.

71 One such region is Antarctica, where data-coverage has been accumulated over decades through
72 many airborne and marine surveys [Golynsky *et al.*, 2018]. Given the lack of outcrop information I
73 Antarctica, this data provides a crucial resource to the understanding of the continental interior,
74 including important aspects such as defining correctly the locations of major tectonic structures [A.
75 R. A. Aitken *et al.*, 2014; Ferraccioli *et al.*, 2011; Tinto *et al.*, 2019], defining sedimentary basins [A. R.
76 A. Aitken *et al.*, 2014; Ferraccioli *et al.*, 2009; Tinto *et al.*, 2019]. The knowledge gained from these
77 surveys are often critical for understanding the tectonics of Gondwana and earlier supercontinents
78 [A. R. A. Aitken *et al.*, 2016; Ruppel *et al.*, 2018], as well as understanding the conditions at the base
79 of the Antarctic Ice Sheet, in particular geothermal heat flux [Martos *et al.*, 2018].

80 Many airborne geophysical data surveys in Antarctica have a sparse and sometimes irregular data
81 distribution, with data collection at a variety of flying heights and over longer time periods than a
82 typical exploration-focused survey, often across multiple years, sometimes with multiple aircraft and
83 instrumentation suites. Flight lines, in most cases, are not closer than 5 km spaced and may be
84 considered sparse, in the sense that the line spacing is typically greater than the source-sensor
85 separation, leading to aliasing in the survey data, at least in the across-line direction [Reid, 1980].
86 Additional complications include logistical considerations surrounding the cost and complexity of
87 installing remote camps, which promotes the collection of data in long flights undertaken from the
88 widely separated permanent research stations. As a consequence, the survey may occur well away
89 from supporting infrastructure, notably geomagnetic base stations (Fig. 1); as flight-time increases,
90 regular aligned grids with close spacings become logistically infeasible. The survey may also traverse
91 changing geomagnetic conditions over these long distances and long flight times, with little
92 opportunity to provide cross-validation. Finally, the need to combine multiple forms of data in one
93 platform (often, surface mapping lidar, ice penetrating radar, gravity and magnetic data) leads to
94 further compromises in flight-design and collection procedures. These data are not well-suited to
95 conventional data processing approaches, and a different approach is necessary to generate truly
96 representative data products, and to maximise benefit to interpretation.

97 In this paper a data correction workflow is developed and tested, seeking to tackle the specific
98 challenges of sparse and four dimensional data. The aim is to reduce, as far as possible, physically
99 predictable spatio-temporal influences on the data before more pragmatic data adjustment
100 procedures are applied. In particular, with a sparse 4D survey, the assumed inter-line relationships
101 that underpin intersection-based or neighbour-based levelling are not necessarily valid. Finally, we
102 seek a workflow that has minimal human data-value decisions, that is largely automated and that
103 can accommodate new data being added with minimal re-adjustment to existing data. This allows an
104 update at the end of each campaign, or in the case of a compilation, updating as new surveys are
105 added to the database. We apply this approach to a major airborne magnetic dataset from

106 Antarctica, ICECAP [A. R. A. Aitken et al., 2014; Blankenship et al., 2011, updated 2013], which
107 typifies the problems listed above.

108 A particular consideration is to maximise the value of these data for subsurface geological
109 interpretation and modelling to contribute knowledge of subglacial geology. Applications in
110 Antarctica include constraining knowledge of past and current ice sheet states, and in particular to
111 enable the mapping of sedimentary basins [A. R. A. Aitken et al., 2014; Ferraccioli et al., 2009], sub-
112 ice-shelf cavities and lakes [Greenbaum et al., 2015; Tinto et al., 2019], and the identification of
113 potentially high heat flux areas [Carson et al., 2014; Martos et al., 2018].

114 **2 ICECAP data**

115 The ICECAP data used here span surveys conducted in two multi-year stages. The first stage (ICECAP-
116 I) includes campaigns from the 2008-2009 season to the 2012-2013 season [Blankenship et al., 2011,
117 updated 2013], and were previously published in Aitken et al [2014] and included in the ADMAP-2
118 compilation [Golynsky et al., 2018]. The second stage (ICECAP-II) includes here the data from
119 campaigns in the 2015-16 and 2016-2017 seasons [Roberts et al., 2018]. Earlier ICECAP-I data
120 processing focused on deriving an interpretable image, and included conventional steps such as
121 base-station correction, removal of the International Geomagnetic Reference Field (IGRF) and
122 intersection-based levelling [A. R. A. Aitken et al., 2014].

123 All data collection was undertaken from a Basler BT-67 aircraft, registered C-GJKB, owned and
124 operated by Kenn Borek Air, Ltd. A Geometrics 823A Caesium Vapour magnetometer was mounted
125 in a tail boom, while positioning is provided from central, tail and wingtip mounted GPS sensors.
126 Surface elevation data and ice thickness data was generated from UTIG HiCARS and HiCARS-2 ice
127 penetrating radar systems [Blankenship et al., 2012, updated 2013a]. The surface elevation data was
128 supplemented by Riegl laser-altimeter data [Blankenship et al., 2012, updated 2013b]. Survey
129 priorities were different in different seasons, with initially the focus on large-scale coverage through
130 long radial lines, then subsequently a focus on coastal regions in more conventional grid patterns
131 (Fig. 1). Throughout the program satellite-tracks were flown, as were older traverse lines, as well as
132 transit flights and line re-flights. In the data-sparse environment of Antarctica, all these ancillary
133 flights are important to improve coverage.

134 **3 Correction Workflow**

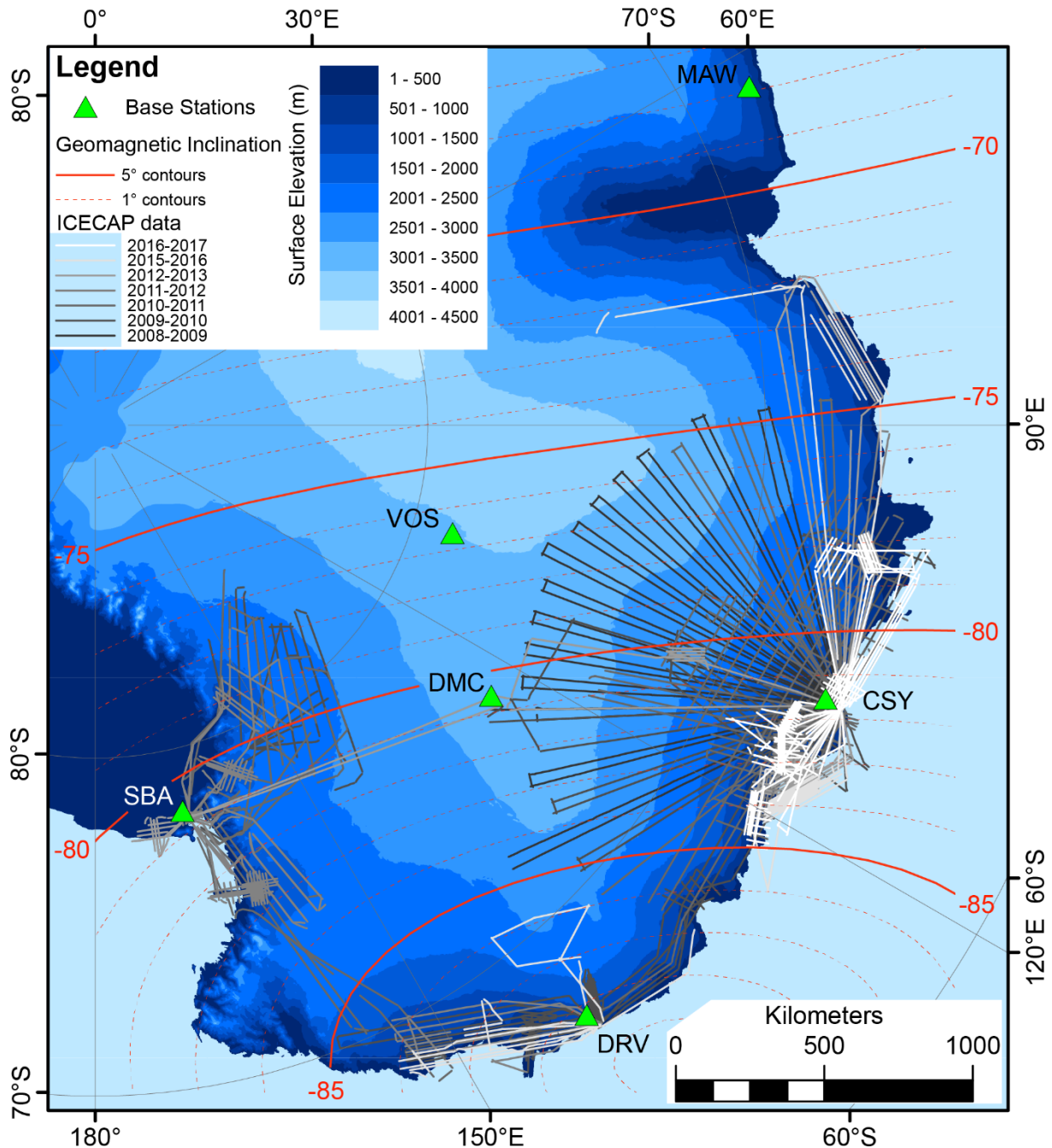
135 The characteristics discussed above lead to a complex data-processing environment demanding, as a
136 particular limitation beyond those of more typical data, the reconciliation of data from different
137 years, different flight heights, different line orientations, at large distances from base stations, and
138 with varying geomagnetic field conditions. Initial data for this study is the raw data with only basic
139 field QC procedures applied [Blankenship et al., 2011, updated 2013; Roberts et al., 2018].

140 The new processing workflow presented here comprises three phases, with increasing data-
141 connectedness (Fig. 2): Phase 1 involves point-by-point operations on individual data points; phase 2
142 includes line-by-line operations on individual lines and phase 3 includes multi-line operations on
143 inter-line relationships.

144 Throughout the workflow, several software packages were used, including Oasis Montaj® for
145 database handling and basic data operations, python, POMME [S. Maus et al., 2010] and escript
146 [Gross et al., 2015]. Only POMME and escript have specific properties, and each is open-source;
147 there is no dependence on proprietary techniques. The new approaches used in this study are
148 described in the supporting information.

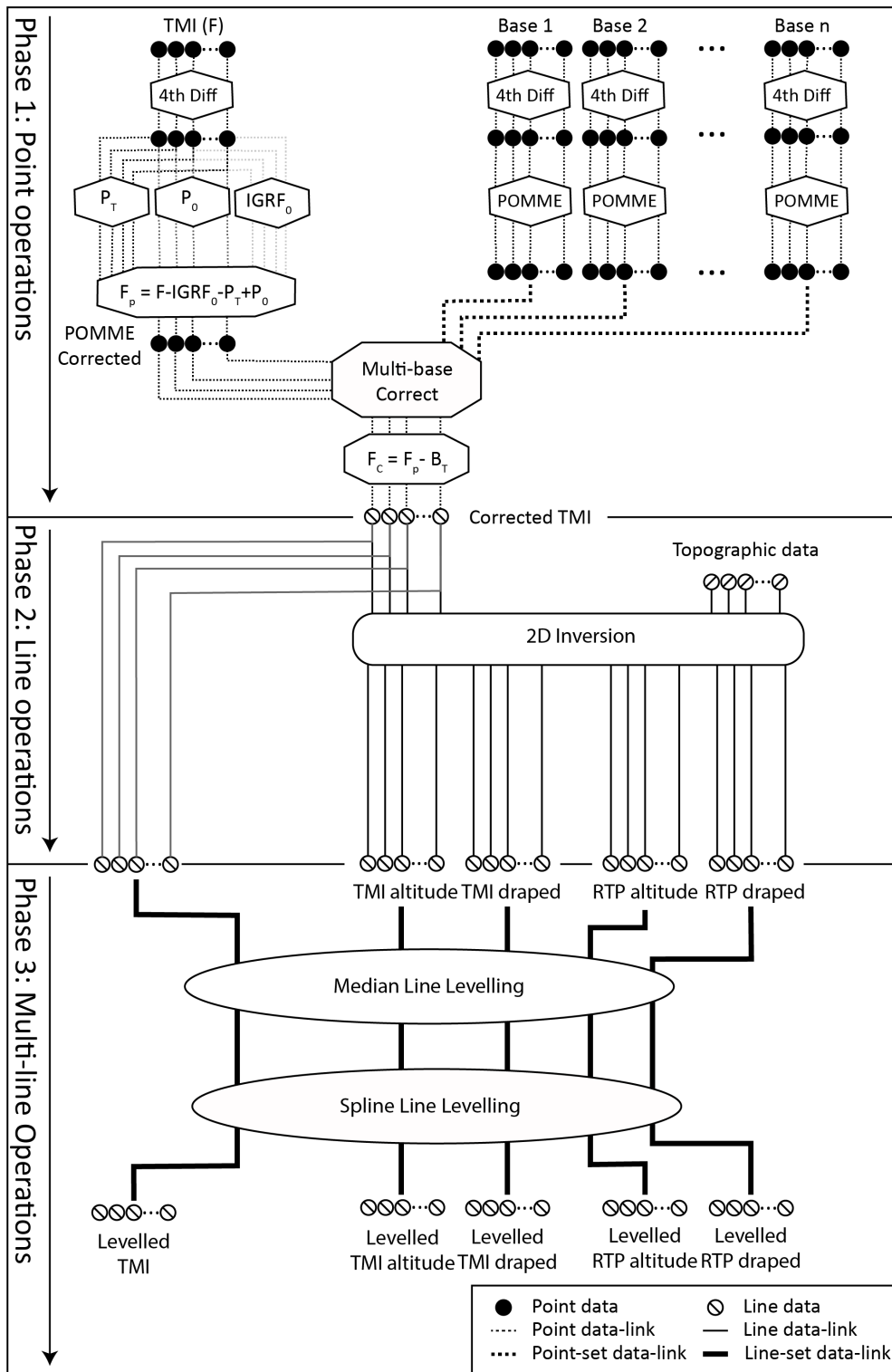
149 3.1 Phase 1 – Point-by-point operations

150 These data-processing steps are derived taking into account the large spatial and temporal scale of
 151 the dataset covering large distances and multiple years. The large volume of data (203 000 line km)
 152 and a desire for consistency and repeatability demanded a semi-automated process with minimal
 153 human intervention. Several steps are included in phase 1 – basic QC and denoising, IGRF removal
 154 [Thébault *et al.*, 2015], correction of spatio-temporal field variations with POMME [S. Maus *et al.*,
 155 2010], and correction of the residual time-varying field with regional base station data.



156

157 Figure 1: ICECAP-I and ICECAP-II Data distribution by season. INTERMAGNET magnetic observatories
 158 are indicated in green with IAGA codes and observatory names: CSY – Casey Station, DMC – Dome C,
 159 DRV – Dumont d’Urville, MAW – Mawson, SBA – Scott Base, VOS – Vostok. Geomagnetic inclination
 160 contours are in red. The ice-sheet and ice-shelf surface is from Bedmap-2 [Fretwell *et al.*, 2013].



161

162 Figure 2: MDCWS-4D processing workflow. The workflow is divided into 3 main phases, each with
 163 greater connectivity of data.

164 3.1.1 Methods

165 3.1.1.1 Data import, QC and de-noising

166 All data were imported from native ASCII text formats into databases, and data were checked for
 167 obviously erroneous values, NaNs, missing data, and other such problems. These were corrected if
 168 possible, or the data omitted from further steps if not feasible. Locally noisy data was accounted for

169 using the fourth difference transform [Hood et al., 1979] applied to the time-series data. In the
170 fourth difference processing, data was excluded where a magnitude threshold (unscaled) of 20 was
171 exceeded. A Dirac delta function of x nT provides a 4th difference magnitude of $6x$, while a Heaviside
172 step function of x nT provides a 4th difference magnitude of $3x$. Correspondingly, the threshold
173 applied will allow single-point “spikes” of up to 3.33 nT and single-interval “steps” of up to 6.67 nT.

174 Following thresholding, an automatic routine was used to correct for minor spikes in the data. The
175 routine looks in the fourth difference transform for a sufficient closeness to the characteristic fourth
176 difference pattern of $0x, +1x, -4x, +6x, -4x, +1x, 0x$, where x is the magnitude of the spike. The need
177 for this correction was identified with a moving window, considering both the numerical defect from
178 this pattern, defined as $|i_{n-2} + i_{n-1}/-4 + i_n/6 + i_{n+1}/-4 + i_{n+2}|$ and the symmetry observed, defined as
179 $(4 \times |(i_{n+1}-i_{n-1})/((i_{n+1}+i_{n-1})/2)| + |(i_{n+2}-i_{n-2})/((i_{n+2}+i_{n-2})/2)|)/5$. If both defect and symmetry were below a
180 tolerance of 0.5, a correction was applied based on $i_n/6$.

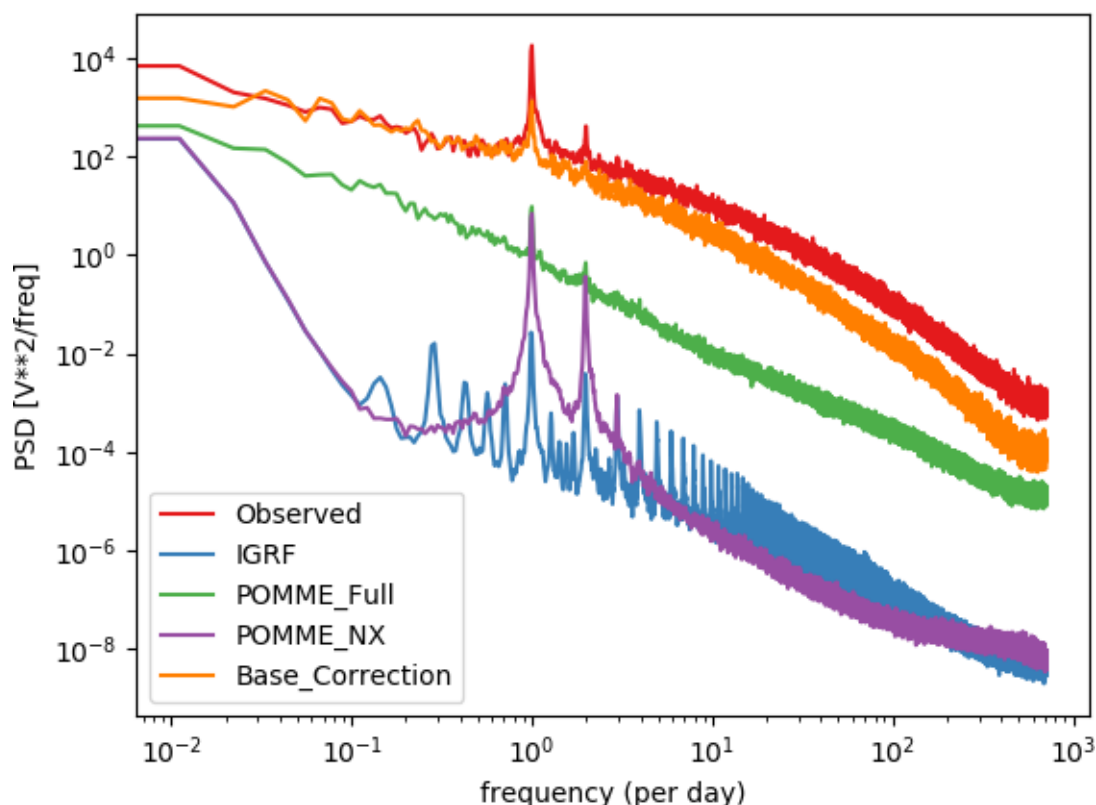
181 A procedure was also run to identify steps based on their own characteristic signature in 4th
182 difference transform, i.e. $0x, 1x, -3x, 3x, -1x, 0x$ where x is a step between stations 3 and 4. Using
183 similar equations as for spikes, the size of the step was recorded, however the removal of steps is
184 more nuanced than spikes, and so they were not corrected for automatically, but are flagged in the
185 database for potential manual correction.

186 3.1.1.2 POMME Geomagnetic Modelling

187 POMME geomagnetic field models attempt to capture in a spherical harmonic model the Earth’s
188 geomagnetic field from the near surface to elevations of several thousand kilometres [S. Maus et al.,
189 2010]. In contrast to the IGRF/DGRF, which accounts for longer-term and long-wavelength magnetic
190 field variations [Thébault et al., 2015], POMME also includes the capacity to include the core,
191 lithospheric magnetospheric and induced fields on much smaller length scales and shorter
192 timescales [S. Maus et al., 2010]. In this study we used the tenth iteration of the model, POMME-10.
193 This model is based on satellite data from the CHAMP (July 2000 – September 2010), Oersted
194 (January 2010 to June 2014), and Swarm (December 2013 to November 2015) satellite missions. For
195 the IGRF we use the 2015 model (12th generation) [Thébault et al., 2015].

196 The required components for POMME modelling were compiled for each data point. These comprise
197 the latitude, longitude and elevation of the data point, and the time of data collection. For best
198 results, several model components are needed that describe the state of the magnetosphere: IMF-
199 By (GSM), IMF-Em (GSM), Est and Ist indices and F10.7. Interplanetary Magnetic Field Data indices
200 obtained from OMNIWEB 1 minute data [King and Papitashvili, 2005], from which the y-component
201 (IMF-By) was extracted in Geocentric Solar Magnetospheric (GSM) coordinates, sampled 35 minutes
202 prior to the data collection time; the merging electric field Em was also derived from this data,
203 sampled 60 minutes prior to data collection time. Hourly Est/Ist indices representing the external
204 and internal components of the magnetospheric disturbance magnetic field [Stefan Maus and
205 Weidelt, 2004] were obtained from the NOAA geomagnetism server, and sampled at the data
206 collection time. Finally the 10.7 centimeter solar flux was obtained from data collected at the
207 Penticton Observatory (F10.7), for which we use the 81-day central average of observed solar flux,
208 sampled 20 months prior to the data collection date [Tapping, 2013]. Est/Ist and F10.7 coverage is
209 complete over the survey period, but the OMNIWEB record has some periods lacking data. Gaps in
210 the IMF-By and IMF-Em records of less than 2 hours were interpolated with a maximum entropy
211 prediction algorithm. This approach maintains noise characteristics similar to the original data. Any
212 remaining gaps were assigned default values of 0 for IMF-By and 0.5 for IMF-Em.

213 POMME is used here as an alternative to the IGRF, seeking to improve the representation of higher
 214 frequency components of the magnetic field in the data correction process. We visualise this using
 215 the long-term record from Scott Base from 2008/07/01 to 2013/06/30 (Fig. 3). Power spectral
 216 density for the full POMME correction for this record is similar to the IGRF at frequencies of 1 per 90
 217 days or lower, but a substantial difference in power spectral density is seen at frequencies > 1 per 10
 218 days. POMME correction with default values for the magnetospheric components (i.e. IMF-By, IMF-
 219 Em, Est, Ist and F10.7) matches the IGRF closely, although providing higher power to diurnal and
 220 semi-diurnal cycles. Although substantially higher powered than the IGRF, the power spectral
 221 density of POMME remains well below the observed signal (Fig. 3).



222
 223 Figure 3: Power Spectral Densities (PSDs) for the Scott Base station record from 2008/07/01 to
 224 2013/06/30, showing PSDs for the observed magnetic field intensity, the IGRF, POMME corrections
 225 with the magnetospheric components (Full) and with default values for these (NX). Also shown is the
 226 base-to-base correction calculated for Scott Base from the other base stations in the region. PSDs
 227 are calculated with Welch's method [*P. Welch, 1967*] using 1-minute data with a window size of 90
 228 days. IGRF data are calculated daily, so are aliased for frequencies above 0.5 per day.

229 3.1.1.3 Multiple Base Station Correction

230 Following the POMME data correction process, an explicit base-station correction is applied to
 231 account for remaining temporal field variations at higher frequencies (Fig. 3). Conventional methods
 232 using a local base station directly are not appropriate here, and so we define a method for the use of
 233 multiple distant base stations. The method accounts for several influences that are not accounted
 234 for in single station base-station procedures: First, it allows for multiple base stations to be included,
 235 for this study up to 6; Second, the procedure smoothly and automatically transitions between base-
 236 stations as the flight-line traverses through space; Third, the correction from each station is inverse-
 237 distance weighted using a power law function, the order of which is able to be specified. Inverse
 238 distance weighting is applied relative to a variable scaling-factor dependent on the furthest included

239 station. Observations distant from any station are minimally corrected, reducing the risk of over-
240 correction, while those close to a station, or stations, will receive stronger corrections. The fourth
241 consideration in the correction is the geomagnetic distance, given by the difference in inclination,
242 and the procedure allows to exclude stations that are geomagnetically distant from the observation
243 (see Fig. 1). Finally, the procedure allows for the vertical damping of base station records,
244 accounting for elevation differences. For this adjustment, a square plate model is used [Telford *et al.*,
245 1990], with a user-specified width – narrower plates provide stronger vertical damping.

246 Large corrections from distant stations are high risk, potentially causing over-correction, and so as a
247 measure of the risk of over-correction from distant stations the “leverage” applied to the correction
248 is calculated. Leverage is defined for each contributing base station as the magnitude of the station
249 correction multiplied by the distance to that station relative to the length scale. Overall leverage is
250 defined by the sum over all included stations. Leverage may be used to exclude high-risk corrections,
251 and as a guide to the quality of the correction.

252 3.1.2 Base Station Data Application

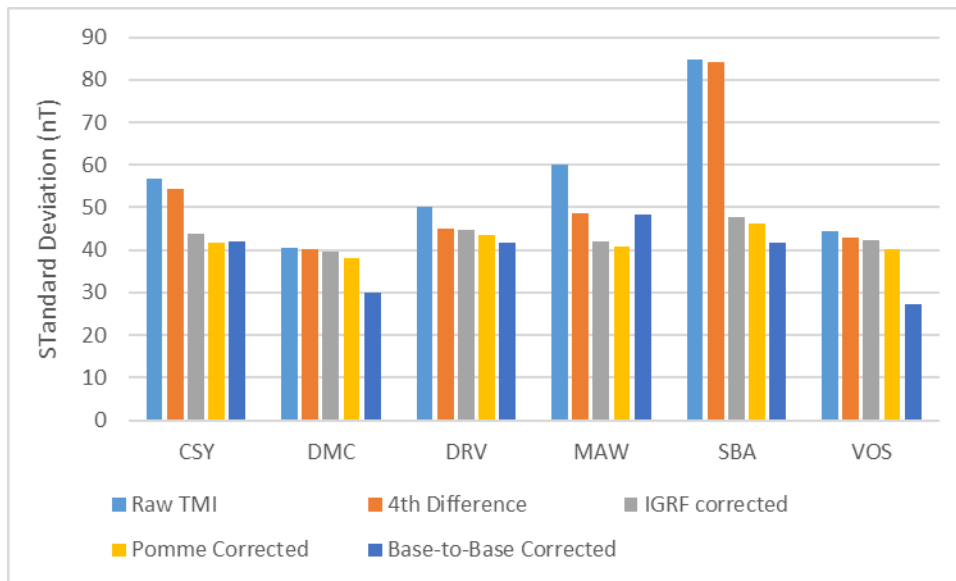
253 Base station data are used here for two purposes. First we use the long-term station records for the
254 period from 2008/07/01 to 2013/06/30, covering the ICECAP-I data collection, to test and validate
255 the point-by-point operations. These also are used to correct the ICECAP-I data. For ICECAP-II, we
256 obtain only the base station data for the specific data collection periods.

257 Base station data were obtained from the International Real-time Magnetic Observatory Network
258 (INTERMAGNET), with 1-minute sampling interval. The observatories available in the region were,
259 Casey station (CSY), Dome C (DMC) Dumont d’Urville (DRV), Mawson (MAW), Scott Base (SBA) and
260 Vostok (VOS). These six stations circumscribe the survey area (Fig. 1).

261 Of these stations, temporal data coverage is variable: DRV, MAW and SBA have complete long-term
262 records with recovery respectively 99.5%, 99.7% and 99.6%. CSY is very nearly complete, excepting a
263 period with no data for 33 days between 2012/10/09 and 2012/11/11, with 100% recovery during
264 station “on” time. DMC covers the complete period, but with a prolonged period with no data
265 (2009/06/30 to 2010/01/01), and lower recovery overall (96.9%). VOS data is available only from
266 2011/01/01 onwards, but has no data between 2012/12/31 and 2013/05/02. 99.6% recovery is
267 achieved during station “on” time. Consequently CSY, DRV, MAW and SBA are consistently available
268 during ICECAP-I surveying, but DMC and VOS had important drop outs in this time. For the ICECAP-II
269 survey periods, recovery was essentially complete for all stations, with over 99.9% recovery rate
270 during station “on” time. DMC was not operational from 2015/12/28 to 2016/01/07, however.

271 The 4th difference noise reduction measures reduced the bulk long-term noisiness of all stations, as
272 indicated by the standard deviation (Fig. 4). Small reductions are seen at CSY, DMC, VOS and SBA, due
273 to the loss of small amounts of noisy data, < 2%, and only minor corrections applied. DRV and MAW
274 saw larger reductions due to the loss of substantial amounts of data, 12% data loss at MAW and 8%
275 at DRV.

276 For all base station records a reduction in the variability of the signal is seen following correction for
277 POMME predictions, but with varying effectiveness (Fig. 4). Only small reductions in variability are
278 seen for DRV of -1.7 nT (3.8%), for DMC of -2.3 nT (5.7%) and for VOS of -2.8 nT (6.5%). For DMC and
279 VOS, this likely reflects their high altitude, whereas the effectiveness of POMME for DRV may be
280 restricted by its position near the pole. Substantially greater variability reductions are seen for MAW
281 of -7.8 nT (16.0%), for CSY of -12.7 nT (23.3%) and for SBA of -37.9 nT (45.1%).



282

283 Figure 4: Base Station signal variability reductions for long-term base station records with the
 284 applied point-by-point corrections. Variability is expressed as the standard deviation of the entire
 285 long-term record, from 2008/07/01 to 2013/06/30, in nT. Base-to-Base and IGRF corrections are not
 286 part of the base-station processing workflow, but are shown to indicate effectiveness.

287 Inter-base corrections are not part of the correction workflow for base station data (Fig 2) however
 288 we apply this here to the long term data records to establish the effectiveness of the method, and to
 289 optimise the parameters. For each base station record, we use the records from the other five
 290 stations to attempt to correct for the deficit in correction, especially at high frequencies. Flight data
 291 are situated in between stations, and so this represents a “worst-case” scenario in terms of
 292 distances between stations. Relative to the POMME-corrected data, substantial reductions in
 293 variability are made for VOS of -12.7 nT (31.2%) and for DMC of -7.9 nT (20.8%). These stations are
 294 close together, and have similar geomagnetic characteristics. Smaller variability reductions are made
 295 for SBA of -4.5 nT (9.7%) and DRV of -1.8 nT (4.1%), while CSY saw a slight increase in variability
 296 overall, of 0.4 nT (1%). Mawson is magnetically, and spatially, quite distant from the other stations,
 297 and the base-to base data correction fails for this station, with an increase in variability of 7.6 nT
 298 (18.6%). As a consequence of this poor result, for the field data correction, we set the maximum
 299 geomagnetic inclination difference at 10°; this value excludes all stations but VOS and MAW for data
 300 near MAW, while allowing data near DRV to receive corrections from CSY, DMC and SBA.

301 For all stations except MAW, testing suggests that the optimum variability reduction is made by
 302 including the nearest four stations, and by using an inverse distance weighting of order two
 303 (distance squared). These settings were adopted for the field data correction. Vertical damping was
 304 found to reduce, to a small extent, the variability at DMC and VOS, suggesting use for high elevation
 305 data, but otherwise was ineffectual, and was not used with field data.

306 3.1.3 Field Data Application

307 As with Base data, flight-line data were checked for obviously erroneous values, location or time-
 308 tagging issues, NaNs, missing data, cultural effects and other such problems that were corrected if
 309 possible, with the data omitted from further steps if not feasible. The same fourth difference
 310 processing was applied to flight lines, first with a threshold of 20 to remove noisy data, and
 311 despiking, with steps identified but not removed automatically. Very few data were altered as a

312 consequence of this process, and so all subsequent steps used the whole dataset, retaining the
313 potential to mask the results according to these thresholds.

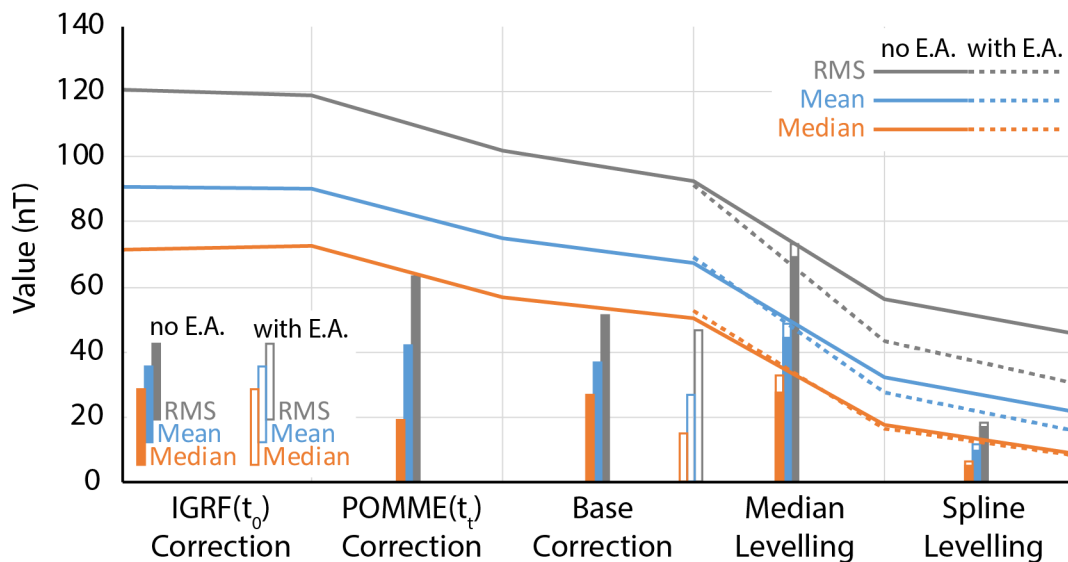
314 For field data, we must also allow for changes in spatial location as well as time. The POMME model
315 resolves spatio-temporal variations in the magnetic field, including some of the lithospheric signal
316 that we wish to retain. To appropriately reduce the field data to the IGRF standard for magnetic
317 anomaly data, we apply a correction that reduces our data to the IGRF-reduced data standard at a
318 particular time, t_0 , in this case the 1st of January 2010.

319 The first step is to remove the IGRF, which we calculate for each data point at time t_0 , using the 12th
320 generation model [Thébault *et al.*, 2015] for all data locations. This accounts only for the spatial
321 variations in the geomagnetic field. Spatio-temporal variations from this standard are defined using
322 POMME. We calculate the full POMME correction at the time of data collection, t_t , and also at the
323 reference time, t_0 . The difference between these provides an additional spatio-temporal
324 geomagnetic correction for each data point, so removing temporal differences in the main field,
325 magnetospheric and lithospheric components. The magnitude of these corrections may be
326 substantial, up to 211.5 nT, with a mean of 41.6 nT, a median of 18.3 nT, and root-mean-square
327 (RMS) of 62.7 nT for the ICECAP data.

328 Base-station corrections were applied to each field data-point using up to 4 base stations, with an
329 inverse-distance-squared weighting, and without any vertical damping. The maximum geomagnetic
330 distance permitted was an inclination difference of 10°, a little less than the difference between VOS
331 and DRV (11.8°). As with the POMME correction, the magnitude of these corrections may be
332 substantial, up to 294.7 nT, with a mean of 36.4 nT, a median of 26.5 nT, and RMS of 50.8 nT.

333 An evaluation of the merit of these data reductions can be made through analysis of residual cross-
334 tie errors. In doing so it must be borne in mind that the survey is four-dimensional. Time differences
335 associated with line intersections vary from several hours to several years, while elevation
336 differences vary from a few metres to over 1 km. The majority of the intersections come from the
337 denser surveys near the coast, therefore, intersection-based measures are not fully representative
338 of the magnitude of error, nor its reduction, much of which occurs in the more remote areas with
339 few line-intersections.

340 Cross-tie errors for the raw TMI data are up to 1325.1 nT, with an RMS error of 120.4 nT, a mean
341 error of 91.0 nT and a median error of 71.4 nT (Fig. 5). As expected, the IGRF correction for spatial
342 variation alone yields very little change to these values, but small reductions are seen, perhaps due
343 to resolving some of the larger elevation-derived discrepancies, and also by reducing the slopes of
344 the data at line intersections. On application of the spatio-temporal POMME correction, the
345 maximum cross-tie error is unchanged, however the RMS, mean and median values are all reduced,
346 to 101.7 nT, 75.1 nT and 56.6 nT respectively. In terms of RMS, this is a reduction of 15% from the
347 raw data. Applying the base-station correction reduces cross-tie errors further, with the RMS
348 reduced to 92.3 nT, the mean to 67.5 nT and the median to 50.3 nT. Overall, Phase-1 of data
349 correction has reduced the cross-tie errors by 30 nT, approximately ~25%.



350

351 Figure 5: Correction magnitudes (columns) and associated cross-tie error reductions (lines) for field
 352 data. Errors at line intersections are interpreted as indicating residual error.

353 3.2 Phase 2 – Line-by-line operations - Elevation Adjustment

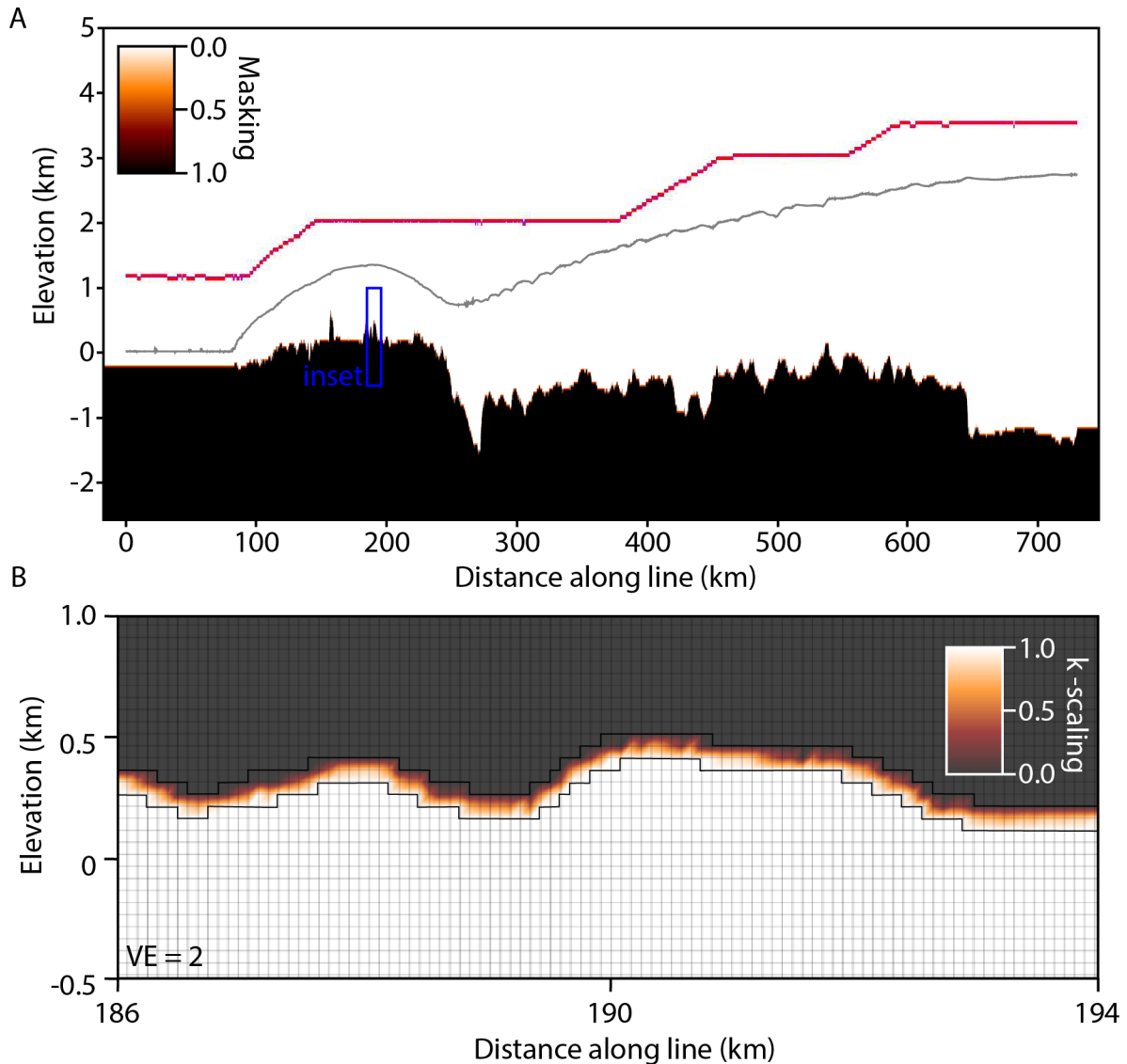
354 In phase 2, we seek to adjust for another major variable in the data, which is differential flying
 355 heights between lines. For ICECAP data, the data are collected at WGS84 ellipsoidal elevations
 356 varying from -43 m to 4199 m. Most of this is dictated by the presence of the ice sheet, but
 357 occasionally differences are due to operational requirements. Source-to-sensor separation distance
 358 is therefore highly varied, both between lines and also along lines, with as much as 5 km variation
 359 being seen on individual lines (e.g. Fig. 6). A common approach to mitigate this is to apply some
 360 variation of wavelength filtering, most commonly field continuation. We consider that this is
 361 problematic due to implicit assumptions regarding the data being collected on a level 2D plane (or
 362 1D line), lack of consideration of the effect of topography and, finally the ability only to be able to
 363 upward continue reliably. Filtering can produce a reliable product at height, but this necessitates the
 364 loss of much valuable information at lower levels.

365 An alternative is to use an equivalent source method, done through the generation of either point
 366 sources or a magnetised layer at the Earth surface to iteratively define the observed magnetic field,
 367 which can then be recomputed in some different place [Cordell, 1992]. A variant of this is to pursue
 368 correction through inversion techniques, which allows for a more nuanced definition of the source,
 369 including sources that are extensive at depth, and have 3D geometries. Furthermore, modern
 370 inversion tools are optimised to deal with large datasets on HPC infrastructure and, while more
 371 computationally expensive, can provide stable results in a time-efficient manner. In this case we
 372 apply an inversion technique, applied using the open-source package escript [Gross et al., 2015].

373 3.2.1 Method

374 Escrip solves the inversion problem using the finite element method. This approach confers several
 375 capabilities that lend itself to our purpose: First, the magnetic field is a continuous function,
 376 piecewise-defined, everywhere within the inversion domain. Consequently, with a single inversion
 377 run, multiple data-realizations can be derived, both above and below the original flight height,
 378 without any recomputation. For example, we may sample the calculated magnetic field at constant
 379 altitudes, and also as “pseudodraped” surveys at various heights above the surface, or on any other
 380 geometry we may choose. A reduced-to-pole realisation can also be derived from the same
 381 inversion, although the field must be recomputed. Second, the inducing magnetic field may

382 smoothly vary within the domain, and everywhere the correct intensity and field orientation can be
 383 used. This is essential for our long lines traversing, in some cases, highly variable geomagnetic
 384 conditions. Third, the method allows data to be reduced to a consistent data-derived standard of fit.
 385 This approach ensures that the model is not over-fitted relative to this data requirement, and stable
 386 results are achieved. Finally, the method is easily automated and while compute-intensive, can be
 387 run as a “set-and-forget” operation on modern HPC infrastructure.



388
 389 Figure 6: Inversion setup for a single line. GL0211a is a coast-perpendicular line extending from Law
 390 Dome inland towards the Aurora Subglacial Basin (location in Fig. 1). A) shows the whole line with
 391 data masked to elements containing data, and the subsurface masking. The surface of the ice sheet
 392 (grey line) is shown here but is not part of the model. Source-sensor separation varies between ~ 1.
 393 5 km to almost 5 km B) An inset showing at fine scale the effective susceptibility scaling (k-scaling)
 394 of the model, with the mesh superimposed. Note the transitional cells which possess a variable k-
 395 scaling, with uniformly 1 beneath, and 0 above. Elements in this case are 50m high and 82 m wide.

396 The inversion approach operates on each line independently, and is automated so as to be able to
 397 be conducted without user intervention. Several steps are undertaken: First the original flight lines,
 398 which may be curved, are cut into straight line-segments, permitting not more than a 45° turn over
 399 10 km. Minimum line-segment length is 20 km. For input to inversion, data are reduced to a

400 common sample frequency of 1 Hz (ca. 80-90m at the typical aircraft velocity). The data file provided
401 to the inversion contains the following information, derived from ICECAP data re-sampled at the
402 magnetic data points: longitude, latitude, along line distance, flight elevation, bed elevation, IGRF
403 field intensity, inclination and declination. Escript has capacity for unstructured meshing, promising
404 much reduced computational requirements, however for this work a regular rectilinear domain with
405 cuboidal elements is used, due to easier automation of the domain building process.

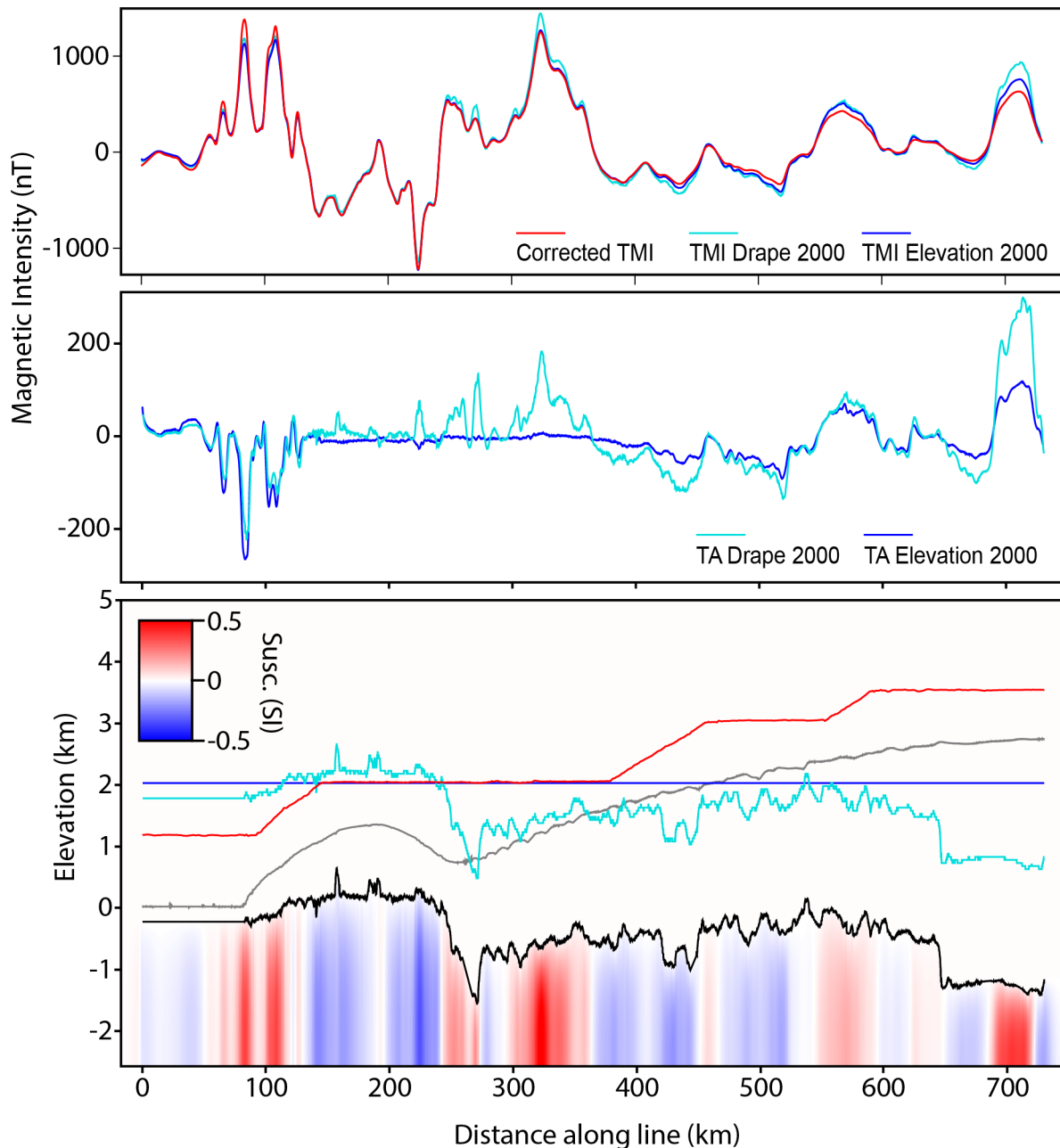
406 First, a 3D inversion domain is built from the data file, in data-defined UVW coordinates, applying
407 suitable padding to the ends, top, base and sides of the data extents. In our case we take the line-
408 segment data file and define vertical (W) extents extending 2.5 km above the highest data elevation,
409 and 1 km below the lowest bed elevation. In the along line direction (U), padding is added to each
410 end of the domain of approximately 2 times the domain height, defined as above. The lateral (V)
411 extent of the domain is 5 times the domain height. The element length (ΔU) is set everywhere to the
412 average data-point interval in the data file (typically ca. 80-90 m), while element height (ΔW) is set
413 to 50 m. In the lateral direction, just 7 elements are used, so the element size (ΔY) is much larger.
414 Inversion therefore is essentially of a 2.5D nature [Rasmussen and Pedersen, 1979].

415 Second, the model is populated with the data. Magnetic data are located in the relevant elements,
416 with the data-function defined at element-centroids only on the central V element. All other
417 functions are defined as continuous functions on element nodes, extensive across all V elements.
418 The solid Earth, within which and only within which we wish to permit susceptibility changes, is
419 defined using a fuzzy set approach: First we define the set of elements that are not entirely above
420 the local surface, to which "solid Earth" membership is assigned. Then, we define the set of
421 elements that are not entirely below the surface, to which "not solid Earth" membership is applied.
422 Finally, for elements that belong to both sets, we re-assign the solid Earth membership value
423 according to the extent to which the element is occupied by the solid Earth. For example for an
424 element extending from 0 to 50 m, if the surface elevation is 25 m, the solid Earth membership value
425 would be 0.5. The susceptibility response of the model is scaled according to the solid Earth
426 membership function. This implementation preserves the volume of the solid earth, but not the
427 shape, so a suitable vertical separation of at least ΔU must be ensured to accommodate the mesh.

428 The model domain is also populated with the values of the inducing magnetic field, as described by
429 the IGRF (here calculated at t_0). The inducing field is piecewise translated into UVW field
430 components, accounting for the line-segment orientation relative to true north (φ_U). φ_U is defined
431 for the entire line-segment, as the arctangent of the longitudinal distance over the latitudinal
432 distance, ensuring quadrant is preserved (numpy.arctan2 function). This avoids introducing noise as
433 a consequence of local deviations from the overall line direction, but for long-lines, curvature is
434 possible relative to the direction of true north. On the longest latitudinal line, likely to be worst
435 affected, the declination discrepancy ranges from -5.5° to 5.8° . Given the 2.5D nature of the models,
436 the, in general, short line-segment and the high magnetic field inclinations, this approximation is not
437 a major source of error in the elevation adjustment calculations.

438 To perform the inversion, the built in magnetic intensity inversion module of escript is called, to
439 generate an approximate solution to the susceptibility required in the subsurface to explain the
440 observed magnetic field intensity variations. We apply the inversion as a series of attempts to solve
441 the problem, beginning with a highly regularized (i.e. smooth) solution, and progressively relaxing
442 the regularization until the target RMS misfit is reached, or until a number of cycles have been
443 completed without a suitable result. The trade-off parameter μ describes the relative importance of

444 data fit to smoothness in the inversion cost function, with larger values emphasising data fit [Gross
445 *et al.*, 2015].



446
447 Figure 7: Data for ASB_JKB0a_GL0211a showing, top panel, the corrected TMI data and TMI
448 realisations at different elevations; the middle panel shows the magnetic adjustments made. The
449 bottom panel shows the susceptibility model, the elevations sampled and also the ice sheet surface
450 and bed elevation.

451 Using the susceptibility solution derived, the associated magnetic field is sampled at the desired
452 locations within the domain. In our case, the field was sampled at two constant elevations, at 2000
453 m and 4000 m elevation, and at two “pseudo-draped” surfaces, 1000 m and 2000 m above the bed
454 surface. The former realisations give a elevation adjusted version of the magnetic data, that is, they
455 have been corrected for the varying flight elevation, but still contain topographic effects from
456 variable bed topography. The latter provide the potential to also correct for the effects of
457 topography, however, they are more prone to instability and error from the often highly variable

458 subglacial topography (see Fig. 7). A reduced to pole product was also generated, recalculating the
459 magnetic field with a polar magnetisation vector.

460 Care is taken not to calculate anomalies within the solid earth, but both constant elevation and
461 pseudodraped models may involve downward adjustment of the survey into the ice, which may also
462 introduce errors into the data. In contrast to frequency-domain downward continuation, the result
463 of the inversion approach is numerically stable for this adjustment. While the amplitudes of existing
464 anomalies will be adjusted, downward-adjusted data will not gain short-wavelength components
465 that may be present in genuine data collected at lower elevation. Upward adjusted data will lose
466 short wavelength components appropriately.

467 3.2.2 Application

468 963 line-segments were modelled. Modelling used the Magnus supercomputer, a Cray XC40,
469 located at the Pawsey Supercomputing Centre located in Perth Western Australia. The automated
470 modelling procedure reads the data for an individual line from the overall database output in ASCII
471 txt format, builds a domain and runs an inversion as described above.

472 In our application the target RMS misfit was 3 nT, and the maximum number of cycles permitted was
473 6, each for up to 50 iterations or until convergence is reached. Convergence in escript occurs when
474 the size of the model update from an iteration is below a certain tolerance factor of the overall
475 model size [Gross *et al.*, 2015]; in this case the tolerance factor was 1×10^{-4} . Convergence does not
476 imply a satisfactory result from the point of view of data misfit. Therefore, multiple attempts may be
477 needed. For several cycles, the model trade-off parameter, μ , was increased by an order of
478 magnitude, beginning at 0.1 up to a maximum of 10,000. At the conclusion of each cycle either the
479 model process terminated, if RMS misfit was satisfactory, or the results were passed into the next
480 cycle.

481 Of the 963 line-segments, 893 satisfactorily reduced RMS misfit to less than 3 nT within 6 cycles of
482 up to 50 iterations. All but 13 lines had residual RMS misfits of less than 10 nT and the worst
483 residual misfit was 29.9 nT. The elevation adjustments made were substantial. For adjustment to a
484 constant elevation of 2000 m, adjustment magnitudes were up to 1874.8 nT, with a mean of 26.6 nT,
485 a median of 14.6 nT, and RMS of 46.3 nT. Despite the substantial change in magnetic field, there was
486 little direct impact on mistie-reduction (Fig. 5).

487 Individual jobs used between 1 and 12 24-cpu compute nodes, running for periods up to several
488 hours. As an example, ASB_JKB0a_GL0211a, a large line with 8900 data points, was completed on 5
489 nodes in 3 hrs and 42 minutes, consuming 445 cpu-hours to achieve a final RMS misfit of 0.89 nT
490 after 4 cycles of iterations. A shorter line, TOT_JKB2n_Y15b, with 1272 data points, was completed
491 on 1 node in 52 minutes, consuming 21 cpu-hours to achieve a final RMS misfit of 2.22 nT after 3
492 cycles of iterations. Model run-time varied with the number of data points, coupled with the
493 complexity of the magnetic field and subglacial topography.

494 3.3 Phase 3 – Multi-line operations - Levelling

495 Following these corrections, the overall cross-tie errors have been reduced by 25%. In the final
496 phase, we apply a two-stage levelling process to account for residual errors following these
497 corrections. Unlike a conventional survey, line-intersections in this data are associated with large
498 differences in time and elevation. Although these differences are adjusted for, we may consider
499 levelling in this case as an attempt to bring independent data into mutual agreement, rather than a
500 correction. Implicitly, preserving the data integrity along the line is more important than ensuring a
501 low crossover error with other lines. Therefore we apply a conservative line-based approach,

502 comprising first a base-level adjustment, and second spline-based levelling. Levelling is applied to
503 the corrected TMI data and to the data adjusted to an elevation of 2000 m.

504 3.3.1 Method

505 The ICECAP data, in common with many sparse, four-dimensional datasets do not everywhere
506 possess a clear hierarchy or ordering of the line sets. Although many of the sub-surveys are flown
507 with distinct orthogonal line sets, these aren't aligned with each other, and furthermore they
508 overlap and are intersected by regional lines of a variety of orientations. Therefore inevitable
509 problems emerge with respect to structuring the levelling approach. Two fundamental choices exist,
510 being network-adjustment methods focusing on loop-closures, or line-based levelling using smooth
511 functions.

512 3.3.1.1 Median Line Levelling

513 In the first stage, we seek to apply only a base-level adjustment to the data, so as not to introduce
514 long-wavelength artefacts. With the ICECAP data, which has no particular line hierarchy, we must
515 first define the hierarchy of lines, to define the order of correction. A new technique is developed,
516 using the median cross-tie error on each line as representative of the adjustment needed.

517 Line-segment intersections are defined by cycling through line-segment pairs, and for each linear
518 line-segment, recording the points on the target line-segment that are within 50 m of a point on the
519 reference line-segments. With the linear line-segments multiple crossings are not possible, and so
520 for each line-segment pair, we seek one value that defines the cross-tie error, recording for the
521 target line the point location, FID and the value adjustment required to match the reference line.

522 Our approach to levelling these lines uses the median mis-tie value from the intersection points to
523 define the optimal correction for each line-segment. It may be the case, due to oblique intersections
524 or where lines are coincident, that more than one point is returned as an intersection for any given
525 line-segment pair. In this case the mean cross-tie error of the intersection points is assigned to the
526 mean XY location of the intersection points, and so only one value is given for each line-segment
527 pair.

528 Adjustments are applied in an iterative fashion. In the algorithm, the line-segments are ordered in
529 "worst-first" order, based on the median cross-tie error for each line-segment. The algorithm adjusts
530 the worst line-segment, and updates all the cross-ties on applicable reference lines. The algorithm
531 then adjusts the second worst line and so on until all lines have been adjusted. Several iterations of
532 this cycle are repeated, testing for convergence to a given standard, defined by the reduction of the
533 highest line-segment median to a given value. The final adjustments are applied line-by-line to the
534 line data.

535 3.3.1.2 Spline-based Levelling

536 Following the median based line-levelling, the data set is able to be addressed with standard
537 levelling techniques. In practice, the optimum levelling approach this stage depends on the desired
538 application and target region. For this study we apply a conservative spline-levelling approach that is
539 appropriate for application to the entire dataset, considering the line-segments still as independent
540 records. For each line-segment, the residual cross-tie errors after median-based levelling are
541 loaded, halved so as to factor in a corresponding adjustment to the reference line, and a tensioned
542 spline is fitted through these points. The points are manually edited to remove occasional erroneous
543 values, and also values that generate sharp features in the spline. This process avoids human
544 decisions over line-segment hierarchy, and ensures no over-correction of the data, at the cost of a
545 systematic under correction.

546 3.3.2 Application

547 For both the corrected TMI data and the elevation adjusted data, median-based levelling was
548 applied to the 963 line-segments, for which 9,488 line-segment pairs were identified. The levelling
549 algorithm was applied with a desired standard of 1 nT and a maximum number of cycles of 20. For
550 both applications, with corrected TMI and elevation-adjusted TMI, convergence was achieved to the
551 data standard. before 20 cycles were completed. 58 line-segments did not possess any intersections
552 and a further 9 adjustments were considered erroneous due to large line-correlated effects being
553 visible in the data. These line-segments were not levelled using the intersection values, but were
554 brought into agreement with the rest of the data by applying a base-level shift derived from the mis-
555 match of the data to a low-resolution (20 km) regional grid of the retained lines, after levelling.

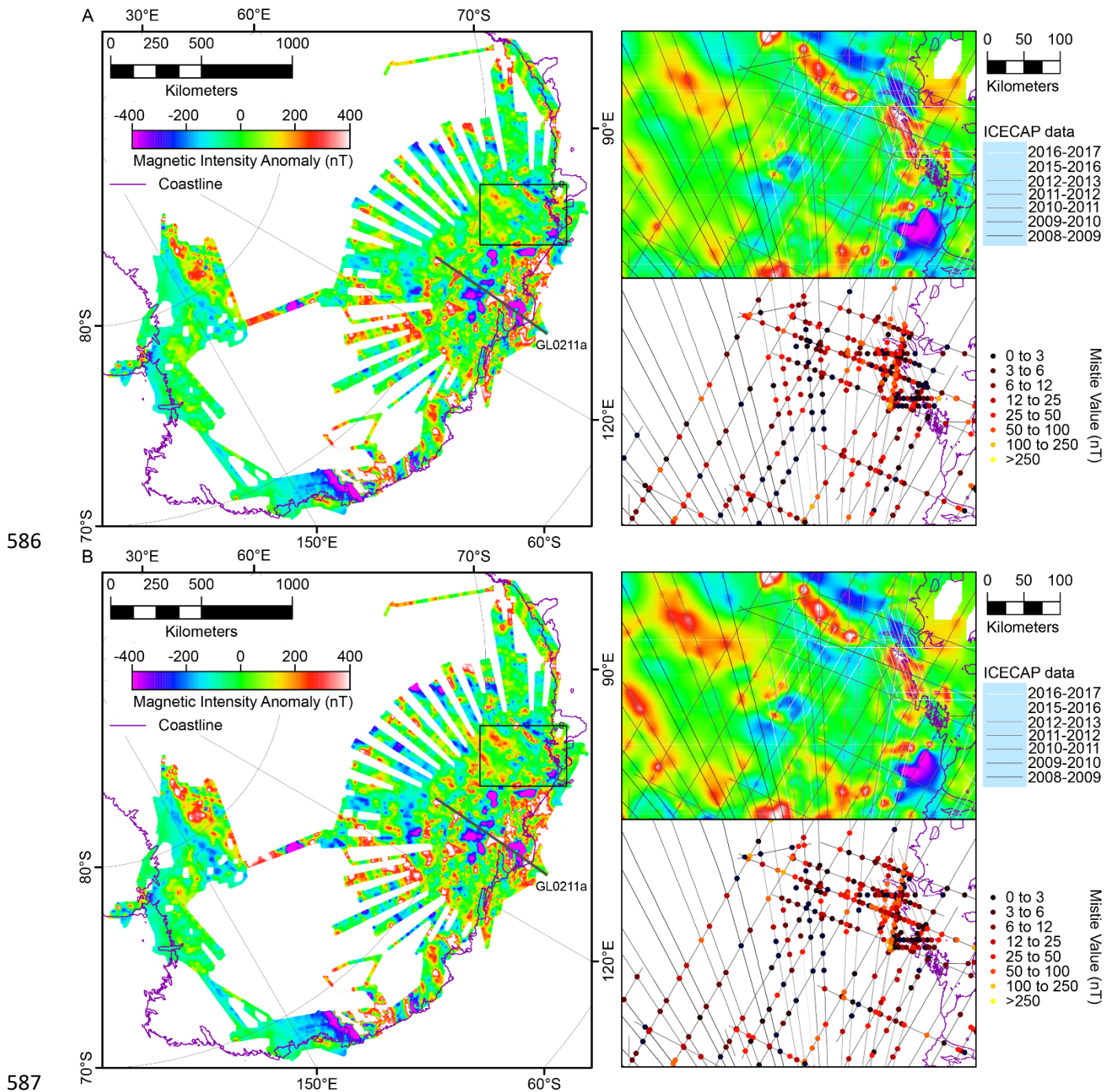
556 Apart from the IGRF removal, median-based line levelling is the most powerful component of the
557 correction process, resulting in substantial changes to the data (see supporting information), and of
558 course reduction in the overall cross-tie error (Fig. 5). For the corrected TMI, the largest adjustment
559 applied through median line levelling was 1247.3 nT, the mean 44.6 nT, the median 27.4 nT and the
560 RMS 68.9 nT. For the elevation adjusted TMI, adjustments were larger, being up to 2113.2 nT, with a
561 mean of 48.1 nT, a median of 32.2 nT and an RMS of 72.8 nT. This difference in magnitude occurs
562 due to the de-meaning process applied during the elevation adjustment; the inversion uses de-
563 meaned data, after which the mean is returned to the data without further adjustment. If the
564 elevation adjustment is not zero-mean, then an error is introduced. The clear result is that, although
565 mis-tie-values overall slightly increased with elevation adjustment, the elevation adjusted data is
566 substantially more internally consistent once base-level adjustments have been applied (Fig. 5).

567 For each data set, B-spline levelling was applied with a tension of 1 and a smoothness of 0.7, giving a
568 very smooth adjustment overall. In the corrected TMI dataset, 17,964 ties were available, of which
569 13,808 were used in levelling. 14 additional line-segments were excluded from the levelling due to
570 erroneous cross-tie values. Along with the lines previously identified as unsuitable, these lines were
571 levelled to a regional grid. With the elevation adjusted data, 17,900 ties were available, of which
572 14,993 were used. In this case 15 line-segments were excluded.

573 For the corrected TMI, the change to the data from the spline-levelling process was less than in all
574 the previous steps, with a maximum adjustment of 152.4 nT, a mean of 9.4 nT, a median of 4.5 nT,
575 and an RMS of 16.3 nT. The residual RMS cross-tie error is reduced to 45.7 nT, the mean to 21.9 nT
576 and the median to 9.1 nT. For the elevation adjusted data, results are similar to slightly better with a
577 maximum adjustment of 131.4 nT, a mean of 11.0 nT, a median of 5.8 nT, and an RMS of 17.8 nT.
578 The residual RMS cross-tie error is reduced to 30.2 nT, the mean to 16.1 nT and the median to 8.1 nT
579 (Fig. 5).

580 4 Results

581 The data processing allows for several products to be generated, although our focus is on the
582 corrected TMI at original flight elevation, and an elevation adjusted dataset for elevations at 2000m
583 above the WGS84 ellipsoid (Fig. 8). The latter is the superior product and has brought out many of
584 the higher amplitude features previously "hidden" beneath thick ice in the inland region. Similarly,
585 some coastal anomalies are relatively subdued.



586

587

588 Figure 8: Fully processed data, in A the corrected TMI; in B the corrected TMI also with elevation
 589 adjustment to 2000m elevation. In each case the left panel shows the overall dataset, while the
 590 insets on the right show a zoomed in view of the western Wilkes Land (top) and the residual mis-ties
 591 (bottom). All images use the same colour-scale. For other steps in the workflow, please refer to the
 592 supporting information.

593 The elevation adjusted data can more safely be used in mapping, and especially so for any
 594 quantitative work that is sensitive to the amplitudes of anomalies, which in previous regional
 595 products are inconsistently defined due to differences in flying height [A. R. A. Aitken *et al.*, 2014;
 596 Golynsky *et al.*, 2018]. For example, in figure 8 (inset) we see much more clearly the sub-linear
 597 anomalies in the inland region, that are now of comparable amplitude to those near the coast,

598 suggesting a similar origin. In the corrected TMI the amplitude of these anomalies is much lower,
599 leading to the potential for misinterpretation.

600 **5 Discussion**

601 5.1 Utility of the results

602 The final cross-tie error in general exceed our target of 3 nT, but are within the error threshold of
603 large regional data-grid compilations, when compared with long survey lines [Milligan *et al.*, 2009]
604 and the dataset is adequately precise for most regional investigations. Further adjustment on the
605 basis of line-intersections would of course reduce these errors. We consider that, due to the
606 incomplete data corrections applied in phase 1 and phase 2, the data remain 4D, and it is not valid to
607 pursue an exact fit through levelling.

608 Given the diverse nature of the ICECAP dataset, additional levelling procedures may be fruitful for
609 specific purposes, for example traditional tie-line/flight line levelling can be applied to the high
610 resolution grid-pattern surveys near the coast; while closed-loop methods may be valuable for the
611 moderate-density regions (e.g. inset, Fig. 8). Our data processing provides a regionally consistent
612 starting point for more targeted investigations at smaller scales.

613 The data, in particular the elevation adjusted data, are consistently processed and have a sufficiently
614 small error threshold to be suitable for careful inclusion in automated and quantitative
615 interpretation methods. The data remain aliased in areas with sparse data; this can only properly be
616 rectified by the collection of new data. Finally, in the data presented here we do not correct for the
617 shape of the topographic surface, and so there are residual effects. For example, in figure 8 (inset)
618 the Denman Glacier trough can be seen as a magnetic low, and the Totten and Moscow University
619 ice shelves also have magnetic lows. At least part of this magnetisation deficit may be due to the
620 low topography, however, geological processes, such as faulting or basin formation, are also
621 plausible causes for reduced magnetisation. A fully topographic corrected model can be re-
622 computed from the inversion model results, if required.

623 5.2 Value of the workflow

624 A crucial question is the value of this approach relative to its cost, in comparison to traditional
625 approaches. For each phase we can define some guidelines as to when this approach is beneficial.
626 We consider first, the reduction of error in the data, but also the capacity of the data to resolve the
627 magnetic structure of the solid earth without bias.

628 5.2.1 Phase-1

629 Point-by-point operations, in general, operate quickly on the data and are quite easily applied, so are
630 relatively low cost. The need to collate and reformat data from widespread sources, including
631 multiple base stations, and the magnetospheric components required for POMME is straightforward
632 but relatively time-consuming. There is also some overhead with the input and output of data to
633 external operations, such as POMME, in comparison to those that are integral to the data processing
634 package, such as the IGRF, although this is offset by the large degree of automation possible. The
635 POMME modelling itself is quite rapid, but may take some time for larger datasets. For example, in
636 our implementation for the 2016/2017 dataset, run in serial on a Linux Workstation, total
637 computation time was 40 minutes for ~266,000 datapoints (17,883 line km at 1 Hz).

638 While it is essential to account for the secular magnetic field variation in a multi-year survey, we may
639 consider if the more complex POMME model provides a substantially more accurate correction than
640 the IGRF calculation. For the long-term base station records, comparison with the daily IGRF
641 correction shows that variability after POMME correction is lower for all stations, but only by 1.2 to

642 2.1 nT. Although the bulk reduction on base station signal variability is not marked in comparison to
643 the IGRF correction (Fig. 4), the numerical difference between POMME and IGRF is however not
644 negligible: The overall differences between the full POMME model and the IGRF model range from -
645 57 nT to 256 nT, with a median magnitude of 38 nT, and with substantial variations seen over a
646 range of timescales, from annual to diurnal. For periods shorter than 90 days, although POMME
647 possesses much greater power spectral density than the IGRF, it remains well below the power
648 spectral density of the data records (Fig. 3). 4D geomagnetic models such as POMME may become
649 higher-powered, and higher resolution, and there is scope for this approach to be more beneficial in
650 the future, especially for data in remote locations far from base stations.

651 For the base station correction, computation time is negligible, and the power spectral density is
652 comparable to the data down to periods of a few hours (Fig. 3). The multiple base station correction,
653 applied between bases over a long-term cycle with four bases and an inverse distance squared
654 scaling, is effective in the main, reducing the residual variability in the long-term base station
655 records, except at MAW and CSY. In comparison, running the same correction with undamped
656 values from only the nearest base station yielded inferior results. For the low-altitude stations, the
657 multi-base correction saw variability reductions over a single base correction of -2.7 nT at CSY, -5.3
658 nT at DRV and -3.7 nT at SBA. DMC, MAW and VOS saw little difference, as in each case the
659 correction is highly dominated by a single station. With field data, the multiple-base-station
660 correction reduces the cross-ties errors in the field data by ~ 10%.

661 Overall, the actions performed in phase-1 generate a ca. 20-50% reduction in variability for the long-
662 term base station records, and a comparable ~25% reduction in the cross-tie errors of the flight data.
663 Substantial changes are made to the data, of the order of tens to hundreds of nT. Our testing
664 suggests that the level of error reduction is in all cases greater than traditional IGRF and single base
665 station corrections, but often not markedly so, with a typical increase in effect of 3-5%.

666 5.2.2 Phase-2

667 Phase-2 includes the geophysical inversion, which is used here to adjust the data to a constant
668 elevation, although other transforms are possible within the inversion algorithm including the
669 calculation of pseudo-draped surveys, reduction to the pole, pseudogravity calculations and
670 topographic corrections. At the same time, the data is implicitly smoothed, due to the smoothness
671 requirements of the inversion. In a more conventional processing workflow, fourier-domain filtering
672 is commonly used to perform these tasks, however alternatives such as equivalent point source
673 methods may also be used.

674 The inversion process is substantially more complex and time-consuming than simple filtering,
675 however it is free from theoretical assumptions inherent to the frequency domain approach, most
676 notably the assumption that the potential field is initially sampled on a plane (or line in 2D), rather
677 than a complexly shaped surface. The method is also superior to equivalent source methods in that
678 the recovered susceptibility distribution is smooth, has a depth extent, and involves off-profile
679 magnetisation, albeit in a limited way. A stable mode of downward continuation is enabled,
680 although it must be remembered that this will not generate new short-wavelength information,
681 except in the case of magnetisation of rough topography.

682 Our results show that the elevation adjustment generates notable improvement to the magnetic
683 data, with substantially stronger and more consistent definition of the anomalies beneath the thick
684 ice of interior Antarctica. In addition, while a direct reduction in cross-tie error was not seen, the
685 elevation adjusted data was distinctly superior to unadjusted data after levelling, with RMS error
686 reduced by 34%, the mean by 26% and the median by 11%. The variability of the residual cross-tie

687 errors is also reduced, with the standard deviation 36% less after elevation adjustment. The
688 elevation adjustment therefore has substantially mitigated the effect of the more extreme cross-tie
689 errors.

690 5.2.3 Phase-3

691 Despite the preceding adjustments, the data retain 4D characteristics, and the applied levelling
692 procedure is intended to be conservative, preserving the integrity of the individual lines, but
693 accounting for inconsistencies as identified by cross-tie errors. In terms of the impact on cross-tie
694 errors, the median-based line adjustment is the most impactful part of the workflow. While applying
695 a base-level adjustment is a purely numerical adjustment, it is a commonly accepted part of any data
696 integration exercise, whether with grids or line data [*Minty et al.*, 2003]. The cost of application is
697 low, as the levelling algorithm runs in seconds. The main advantage of the approach is that there is
698 no requirement for a predefined line order or hierarchy, nor the need for an operator to make
699 decisions about which lines need adjustment. While the median is a conservative choice, avoiding
700 over-correction, it is in some cases biased by the uneven distribution of intersections.

701 Spline interpolation, although a very common and robust interpolation procedure, has no physical
702 basis as a correction to magnetic data. Because it makes changes to the relative intensity anomalies
703 along each line, the spline levelling should be applied only once cross-tie errors are minimised. In our
704 case the spline levelling is the smallest magnitude correction, in terms of nT, with a mean magnitude
705 of ~10 nT and a median magnitude of ~5 nT. Manual editing of problematic cross-ties makes this
706 one of the more labour intensive parts of the workflow.

707 The final RMS cross-tie error following phase 3 is 45.7 nT for the corrected TMI and 30.2 for the
708 elevation adjusted data set; the means are 21.9 nT and 16.1 respectively, and the medians are 9.1 nT
709 and 8.1 nT. Phase three has contributed the largest share of the cross-tie error reduction, most of
710 this through the median-based line levelling.

711 5.3 Residual Errors

712 Following this data correction workflow, the magnitude of error reduction, as defined by cross-tie
713 errors is substantial. For the corrected TMI data, RMS error is reduced by 62%, with 76% reduction
714 of the mean error, and 87% reduction of the median error. For the elevation-adjusted data, greater
715 reductions are seen, by 75% (RMS) 82% (mean) and 89% (median), indicating the effect of the
716 elevation adjustment. Despite these reductions, absolute values of mis-tie errors remain above our
717 target precision of 3 nT. Residual errors are concentrated on several problematic lines, with residual
718 cross-tie errors also concentrated near the peaks or troughs of high amplitude anomalies, or at
719 regions of high gradient (Fig. 8). Further levelling may reconcile these errors, but the value of this
720 process may be disputed, given the assumption that the 4D data are satisfactorily reduced to 2D
721 prior to leveling. For a greater reduction to residual error, we may look more closely at our earlier
722 corrections to the data, which are in their nature systematically inadequate.

723 Phase 1 corrections are systematically underpowered with respect to the signal they are intended to
724 correct (Fig. 3). This situation may improve as geomagnetic models like POMME become higher-
725 powered, in particular for shorter periods, due to the inclusion of more detailed magnetic
726 information [*S. Maus et al.*, 2010]. The base station correction, which in this case relies on quite
727 distant stations, often with incomplete records, has a relatively limited effect on the data, and, in
728 our inter base-station test is inadequate with respect to removing diurnal and sub-diurnal intensity
729 variations. An improvement to this part of the process demands a new approach to resolving four-
730 dimensional geomagnetic conditions.

731 Elevation differences are in principle accounted for by the inversion process, however, while
732 anomaly amplitudes are corrected, short-wavelength signals are missing in cases where the
733 elevation is adjusted downwards. Therefore, high-elevation lines, where they intersect low-elevation
734 lines, are not fully compatible, especially if the signal is rough at low elevations (Fig. 8). The inversion
735 process is also not uniformly precise and, where 3D anomalies are involved, the 2.5D model
736 structure may misrepresent the source geometry. Remanent magnetisation is also not accounted
737 for.

738 **6 Conclusions**

739 Our workflow to process data seeks to correct for several systemic errors in magnetic data
740 correction that especially may have impact on sparse, four-dimensional surveys conducted across
741 multiple years in remote environments. The workflow includes three phases considering data as
742 individual points, lines and then sets of lines. With long-term base-station data we show that point-
743 by-point corrections are effective in reducing the variability of the signal by 25 to 50 %, with a similar
744 but slightly smaller effect on reducing cross-tie errors at line intersections. These corrections are
745 superior to a traditional workflow, however the numerical error-reduction is not marked.

746 Phase 2 adjusts for differences in data-collection elevation, adjusting all data to an elevation of 2000
747 m. This step is effective in increasing the relative amplitudes of anomalies in inland locations, where
748 they are buried beneath thick ice. A direct effect on cross-tie errors was not seen, however, the
749 elevation adjusted data saw much larger error-reductions in later levelling, indicating superior data
750 consistency. Although computationally intensive, the inversion process is superior to filtering
751 approaches in that anomalies can be reliably downward adjusted.

752 Phase 3 constitutes the line-based levelling of the data, for which a median-based base-level
753 adjustment was highly effective in reducing cross-tie errors using a rapid approach, requiring little
754 human intervention. Spline-levelling was less effective, but reduced further the relatively small
755 residual errors in the data.

756 The final results of this workflow [A.R.A. Aitken and Nigro Rodrigues Alves Ramos, 2019], while still
757 not of comparable precision to tightly constrained HRAM datasets, reduced the errors by up to 89%.
758 Confidence and interpretability is improved compared to previous ICECAP data processing [A. R. A.
759 Aitken *et al.*, 2014]. In particular, through elevation adjustment, the data in inland regions is brought
760 to a similar standard to the coastal regions and can be interpreted without systemic bias. This
761 includes the use in automated procedures, in particular those that depend on anomaly amplitudes.
762 The improved data allow for new analysis to undertake more comprehensive tectonic and glacio-
763 tectonic research in the region.

764 **7 Acknowledgements**

765 This research was supported through the Australian Antarctic Science Program project grant 4460.
766 ICECAP and ICECAP-II data collection was supported through the Australian Antarctic Science
767 Program project grants 3103, 4077 and 4346. This work was supported by resources provided by the
768 Pawsey Supercomputing Centre with funding from the Australian Government and the Government
769 of Western Australia. We thanks reviewers for providing valuable comments. The data presented in
770 this work is available from the Australian Antarctic Data centre
771 (<http://dx.doi.org/doi:10.26179/5e015bb8dce7f>).

772 **8 References**

- 773 Aitken, A. R. A., P. G. Betts, D. A. Young, D. D. Blankenship, J. L. Roberts, and M. J. Siegert (2016), The
774 Australo-Antarctic Columbia to Gondwana transition, *Gondwana Research*, 29(0), 136-152,
775 doi:<http://dx.doi.org/10.1016/j.gr.2014.10.019>.
- 776 Aitken, A. R. A., and L. Nigro Rodrigues Alves Ramos (2019), Reprocessed Magnetic Data from
777 ICECAP-I and ICECAP-II, 2008/2009 to 2016/2017, Ver. 1, edited, Australian Antarctic Data Centre,
778 doi:10.26179/5e015bb8dce7f.
- 779 Aitken, A. R. A., D. A. Young, F. Ferraccioli, P. G. Betts, J. S. Greenbaum, T. G. Richter, J. L. Roberts, D.
780 D. Blankenship, and M. J. Siegert (2014), The subglacial geology of Wilkes Land, East Antarctica,
781 *Geophysical Research Letters*, 2014GL059405, doi:10.1002/2014GL059405.
- 782 Behrendt, J. C., and C. S. Watorson (1970), Aeromagnetic and gravity investigations of the coastal
783 area and continental shelf of Liberia, West Africa, and their relation to Continental Drift, *Bulletin of*
784 *the Geological Society of America*, 81(12), 3563-3574, doi:10.1130/0016-
785 7606(1970)81[3563:AAGIOT]2.0.CO;2.
- 786 Blankenship, D. D., S. D. Kempf, and D. A. Young (2011, updated 2013), IceBridge Geometrics 823A
787 Cesium Magnetometer L2 Geolocated Magnetic Anomalies, Version 1, edited, NASA National Snow
788 and Ice Data Center Distributed Active Archive Center, Boulder, Colorado USA.,
789 doi:<http://dx.doi.org/10.5067/TO7WLC72UMAQ>.
- 790 Blankenship, D. D., S. D. Kempf, and D. A. Young (2012, updated 2013a), IceBridge HiCARS 2 L2
791 Geolocated Ice Thickness, Version 1, edited, NASA National Snow and Ice Data Center Distributed
792 Active Archive Center., Boulder, Colorado USA., doi: <http://dx.doi.org/10.5067/9EBR2TOVXUDG>.
- 793 Blankenship, D. D., S. D. Kempf, D. A. Young, J. L. Roberts, T. D. Van Ommen, R. Forsberg, M. J.
794 Siegert, S. J. Palmer, and J. A. Dowdeswell (2012, updated 2013b), IceBridge Riegl Laser Altimeter L2
795 Geolocated Surface Elevation Triplets, Version 1, edited, NASA National Snow and Ice Data Center
796 Distributed Active Archive Center. , Boulder, Colorado USA.,
797 doi:<http://dx.doi.org/10.5067/JV9DENETK13E>.
- 798 Carson, C. J., S. McLaren, J. L. Roberts, S. D. Boger, and D. D. Blankenship (2014), Hot rocks in a cold
799 place: High sub-glacial heat flow in East Antarctica, *Journal of the Geological Society*, 171(1), 9-12.
- 800 Cordell, L. (1992), A scattered equivalent-source method for interpolation and gridding of potential-
801 field data in three dimensions, *Geophysics*, 57(4), 629-636.
- 802 Ferraccioli, F., E. Armadillo, T. Jordan, E. Bozzo, and H. Corr (2009), Aeromagnetic exploration over
803 the East Antarctic Ice Sheet: A new view of the Wilkes Subglacial Basin, *Tectonophysics*, 478(1-2), 62-
804 77.
- 805 Ferraccioli, F., C. A. Finn, T. A. Jordan, R. E. Bell, L. M. Anderson, and D. Damaske (2011), East
806 Antarctic rifting triggers uplift of the Gamburtsev Mountains, *Nature*, 479(7373), 388-392.
- 807 Fretwell, P., et al. (2013), Bedmap2: Improved ice bed, surface and thickness datasets for Antarctica,
808 *Cryosphere*, 7(1), 375-393, doi:10.5194/tc-7-375-2013.
- 809 Golynsky, A. V., et al. (2018), New Magnetic Anomaly Map of the Antarctic, *Geophysical Research*
810 *Letters*, 45(13), 6437-6449, doi:10.1029/2018gl078153.
- 811 Greenbaum, J. S., et al. (2015), Ocean access to a cavity beneath Totten Glacier in East Antarctica,
812 *Nature Geoscience*, 8(4), 294-298, doi:10.1038/ngeo2388.
- 813 Gross, L., C. Altinay, and S. Shaw (2015), Inversion of potential field data using the finite element
814 method on parallel computers, *Computers & Geosciences*, 84(Supplement C), 61-71,
815 doi:<https://doi.org/10.1016/j.cageo.2015.08.011>.

816 Hood, P. J., M. T. Holroyd, and P. H. McGrath (1979), Magnetic methods applied to base metal
817 exploration, in *Geophysics and Geochemistry in the Search for Metallic Ores*, edited by P. J. Hood, pp.
818 77-104, Geological Survey of Canada, Economic Geology Report 31.

819 King, J. H., and N. E. Papitashvili (2005), Solar wind spatial scales in and comparisons of hourly Wind
820 and ACE plasma and magnetic field data, *Journal of Geophysical Research: Space Physics*, 110(A2),
821 doi:10.1029/2004ja010649.

822 Martos, Y. M., M. Catalan, T. A. Jordan, A. Golynsky, D. Golynsky, G. Eagles, and D. G. Vaughan
823 (2018), Heat flux distribution of Antarctica unveiled.

824 Maus, S., C. Manoj, J. Rauberg, I. Michaelis, and H. Lühr (2010), NOAA/NGDC candidate models for
825 the 11th generation International Geomagnetic Reference Field and the concurrent release of the
826 6th generation Pomme magnetic model, *Earth, Planets and Space*, 62(10), 729-735.

827 Maus, S., and P. Weidelt (2004), Separating the magnetospheric disturbance magnetic field into
828 external and transient internal contributions using a 1D conductivity model of the Earth, *Geophysical
829 Research Letters*, 31(12), doi:10.1029/2004gl020232.

830 Milligan, P., B. Minty, M. Richardson, and R. Franklin (2009), The Australia-wide airborne geophysical
831 survey - accurate continental magnetic coverage, *ASEG Extended Abstracts*, 2009(1), 1-9,
832 doi:<https://doi.org/10.1071/ASEG2009AB075>.

833 Minty, B. R. S., P. R. Milligan, A. P. J. Luyendyk, and T. Mackey (2003), Merging airborne magnetic
834 surveys into continental-scale compilations, *Geophysics*, 68(3), 988-995.

835 Nabighian, M. N., V. J. S. Grauch, R. O. Hansen, T. R. LaFehr, Y. Li, J. W. Peirce, J. D. Phillips, and M. E.
836 Ruder (2005), The historical development of the magnetic method in exploration, *Geophysics*, 70(6),
837 33-61.

838 P. Welch (1967), The use of fast Fourier transform for the estimation of power spectra: A method
839 based on time averaging over short, modified periodograms in *IEEE Transactions on Audio and
840 Electroacoustics*, 15(2), 70-73.

841 Rasmussen, R., and L. B. Pedersen (1979), End corrections in potential field modeling, *Geophysical
842 Prospecting*, 27(4), 749-760.

843 Reid, A. B. (1980), Aeromagnetic survey design, *Geophysics*, 45(5), 973-976.

844 Roberts, J. L., D. D. Blankenship, J. S. Greenbaum, L. H. Beem, S. D. Kempf, D. A. Young, T. D. Richter,
845 T. G. Van Ommen, and E. Le Meur (2018), EAGLE/ICECAP II GEOPHYSICAL OBSERVATIONS (SURFACE
846 AND BED ELEVATION, ICE THICKNESS, GRAVITY DISTURBANCE AND MAGNETIC ANOMALIES), Ver, 1,
847 edited, Australian Antarctic Data Centre, doi:<http://dx.doi.org/doi:10.26179/5bcfffdabcf92>.

848 Ruppel, A., J. Jacobs, G. Eagles, A. Läufer, and W. Jokat (2018), New geophysical data from a key
849 region in East Antarctica: Estimates for the spatial extent of the Tonian Oceanic Arc Super Terrane
850 (TOAST), *Gondwana Research*, 59, 97-107, doi:<https://doi.org/10.1016/j.gr.2018.02.019>.

851 Tapping, K. F. (2013), The 10.7 cm solar radio flux (F10.7), *Space Weather*, 11(7), 394-406,
852 doi:10.1002/swe.20064.

853 Telford, W. M., L. P. Geldart, and R. E. Sheriff (1990), *Applied Geophysics Second Edition*, 770 pp.,
854 Cambridge University Press.

855 Thébault, E., et al. (2015), International Geomagnetic Reference Field: the 12th generation, *Earth,
856 Planets and Space*, 67(1), 79, doi:10.1186/s40623-015-0228-9.

857 Tinto, K. J., et al. (2019), Ross Ice Shelf response to climate driven by the tectonic imprint on seafloor
858 bathymetry, *Nature Geoscience*, 12(6), 441-449, doi:10.1038/s41561-019-0370-2.

859 Vine, F. J., and D. H. Matthews (1963), Magnetic anomalies over oceanic ridges, *Nature*, 199(4897),
860 947-949.
861